Available online at www.sciencedirect.com
SCIENCE DIRECT®
International Journal of Heat and Mass Transfer 47 (2004) 1731–1743
International Journal of HEAT and MASS TRANSFER
www.elsevier.com/locate/ijhmt

Spatially-resolved heat transfer and flow structure in a rectangular channel with pin fins

S.Y. Won, G.I. Mahmood, P.M. Ligrani *

Convective Heat Transfer Laboratory, Department of Mechanical Engineering, University of Utah, 50 S. Central Campus Drive, MEB 2274, Salt Lake City, UT 84112-9208, USA

Received 30 January 2003; received in revised form 17 October 2003

Abstract

Spatially-resolved Nusselt numbers and flow structural characteristics are presented for a stationary channel with an aspect ratio of 8 and a staggered array of pin fins between two of the surfaces. Local Nusselt numbers, measured on one endwall, are highest beneath primary and secondary horseshoe vortices located just upstream of individual pins, beneath pin wakes, and downstream of the pins, in regions where shear layers are positioned between the wakes behind the pins and the higher speed flow away from an individual pin. Also important are intense, highly unsteady secondary flows and vortex pairs (evident in flow visualizations and time-averaged surveys), which increase secondary advection and turbulent transport over the entire channel cross-section.

1. Introduction

When employed for internal cooling, pin fins or pedestals are generally arranged into arrays, and extend between two opposite walls of an internal cooling passage. Pin fins are generally used in the parts of turbine airfoils where higher levels of heat transfer augmentation are required and where high pressure drops are tolerated, and in many cases, even desired. Trailing edges of airfoils and midspan regions of airfoils sometimes fall into this category. Pin fins are effective for allowing the pressure throughout most of the cooling circuit to remain high, while providing the necessary restriction near the trailing edge, to limit the coolant consumption to the desired level.

The large majority of existing pin fin investigations only focus on heat or mass transfer. Considered are the influences of pin geometry, pin materials, pin fin array configuration, channel geometry, different Reynolds numbers, and other parameters. Only a few recent studies examine fluid flow characteristics through passages with pin fins. Of the earlier *heat transfer* investigations, Zukauskas [1], Sparrow et al. [2], Metzger and Haley [3], and Metzger et al. [4] report Nusselt numbers on flat surfaces as well as on pin surfaces, and indicate the presence of large overall heat transfer augmentations for certain flow conditions and pin fin array arrangements. Van Fossen [5] presents heat transfer coefficients measured on circular pin fins made of different materials, which are placed in rectangular cross-section channels. Different endwall plate-to-air temperature differences are employed. The Reynolds number dependence of the results is described, along with comparisons with available correlations for constant property conditions. Brigham and Van Fossen [6] report large overall heat transfer and mass transfer augmentations for circular pin fins arranged in in-line and staggered arrays. In another study, Simoneau and Van Fossen [7] measure pin surface heat transfer coefficients and streamwise turbulence intensities as the test section gas temperature varies between 260 and 290 K. The authors describe the effects of changing the number of pin rows.

Later investigations by Lau et al. [8], and McMillin and Lau [9] consider the effects of bleed ejection on heat

* Corresponding author. Tel.: +1-801-581-4240; fax: +1-801-585-9826.
E-mail address: ligrani@eng.utah.edu (P.M. Ligrani).

0017-9310/$ - see front matter © 2003 Elsevier Ltd. All rights reserved.
doi:10.1016/j.ijheatmasstransfer.2003.10.007

Nomenclature

a	streamwise extent of test surface
b	spanwise extent of test surface
d	pin fin diameter
D_h	channel hydraulic diameter
H	channel height
h	heat transfer coefficient based on flat projected area, $\dot{q}''/(T_w - T_m)$
k	thermal conductivity
Nu	local Nusselt number, hD_h/k
Nu_0	baseline Nusselt number in a smooth channel with no pin fins
p	streamwise spacing between pin fin centerlines
p'	streamwise spacing between adjacent pin fins
P	time-averaged local static pressure
Pr	Prandtl number
$\dot{q}''$	surface heat flux
Re_H	Reynolds number based on channel height, $\overline{U}H/v$
Re_{Dh}	Reynolds number based on hydraulic diameter, $\overline{U}D_h/v$
s	spanwise spacing between pin fin centerlines
s'	spanwise spacing between adjacent pin fins
T	local static temperature
$\overline{U}$	streamwise bulk velocity averaged over the channel cross-section
u_x	time-averaged local streamwise velocity
u_z	time-averaged local spanwise velocity
X	streamwise coordinate measured from the test section inlet
Y	normal coordinate measured from the endwall test surface between the pin fins
Z	spanwise coordinate measured from the test surface spanwise centerline

Greek symbol

ω_x	streamwise vorticity

Subscripts

a	ambient value
m	time-averaged, local mixed mean value
o	total or stagnation value
w	local wall value

and mass transfer distributions, and on streamwise pressure variations in a channel with circular pin fins. Chyu [10], Chyu and Goldstein [11], and Chyu et al. [12] measure surface mass transfer coefficients using naphthalene-sublimation measurement techniques. Local and spatially-averaged mass transfer coefficients are reported for different pin fin arrays, which provide evidence of large overall mass transfer augmentations for certain inline and staggered circular arrays. Grannis and Sparrow [13] numerically simulate the two-dimensional flow and pressure fields around diamond-shaped pin fins. Olson [14] describes the behavior of helium flowing through a channel with pins at different wall-to-fluid temperature differences. Presented are normalized pressure drop and wall Nusselt number data as dependent upon Reynolds number and wall heat flux magnitude. The investigators employ a temperature ratio/power law scheme to account for variations of thermophysical properties on measured Nusselt numbers. Chyu [10], Grannis and Sparrow [13], Chyu and Natarajan [15], Chyu et al. [16], Hwang and Lu [17], and Uzol and Camci [18,19] consider the effects of different pin fin shapes on heat transfer and flow in internal passages. A variety of pin fin shapes are considered, including circular [10,15–19], pins with endwall fillets [10], diamond [13,15–17], three-dimensional protruding elements [15], cubic [15,16], and elliptical [18,19]. Of these studies, the one described by Hwang and Lu [17] is especially unique because three pin fin configurations, each arranged in a staggered array, are considered in a trapezoidal duct, both with and without lateral flow ejection.

In comparing heat transfer from the pin fins and endwall, Chyu et al. [12] indicate that, except for the first one or two rows, heat transfer coefficients on circular pin surfaces are consistently higher than values on the endwall by 10–20%. Van Fossen [5] reports a 35% differential, whereas Al Dabagh and Andrews [20] report pin surface heat transfer coefficients which are 15–35% *lower* than endwall values. Chyu et al. [12] further indicate that array-averaged results are "virtually equal to corresponding endwall averages" largely because the endwall often accounts for the majority of the total wetted area.

To determine the capabilities of such heat transfer augmentation devices, spatially-resolved surface Nusselt number data are needed. Also helpful are details of the flow field structure because this aids the development of numerical models and prediction schemes, and because this provides important insight into the flow structural characteristics responsible for local heat transfer coefficient augmentations. However, in spite of the value of heat transfer data, obtained together with friction factor and flow structure data, very few papers present such data together for the internal cooling augmentation devices mentioned. The present paper is aimed at remedying this deficiency for internal passages with pin fins. The results given in the present paper are thus new and unique because of these differences, and because new

spatially-resolved heat transfer and flow structure data are presented and inter-related to each other, something which is impossible for experimental rotating pin fin channel studies. Also discussed are the effects of thermal boundary layer development on local Nusselt number distributions. These results are valuable because the spatial resolution of the heat transfer and flow measurements is much better than provided by pin fin results from other sources.

2. Experimental apparatus and procedures

The overall experimental apparatus for heat transfer measurements (but not the test section) is similar to the one described by Mahmood and Ligrani [21]. A brief description of this apparatus is also presented here.

2.1. Channel and test surface for heat transfer measurements

A schematic of the facility used for heat transfer measurements is shown in Fig. 1a. The air used within the facility is circulated in a closed-loop. One of three circuits is employed, depending upon the Reynolds number and flow rate requirements in the test section. For Reynolds numbers Re_H less than 10,000, a 102 mm pipe is connected to the intake of an ILG Industries 10P type centrifugal blower. For Re_H between 10,000 and 20,000, the same pipe is connected to the intake of a Dayton 7C447 1.0 hp centrifugal blower. For higher Reynolds numbers, a 203 mm pipe is employed with a

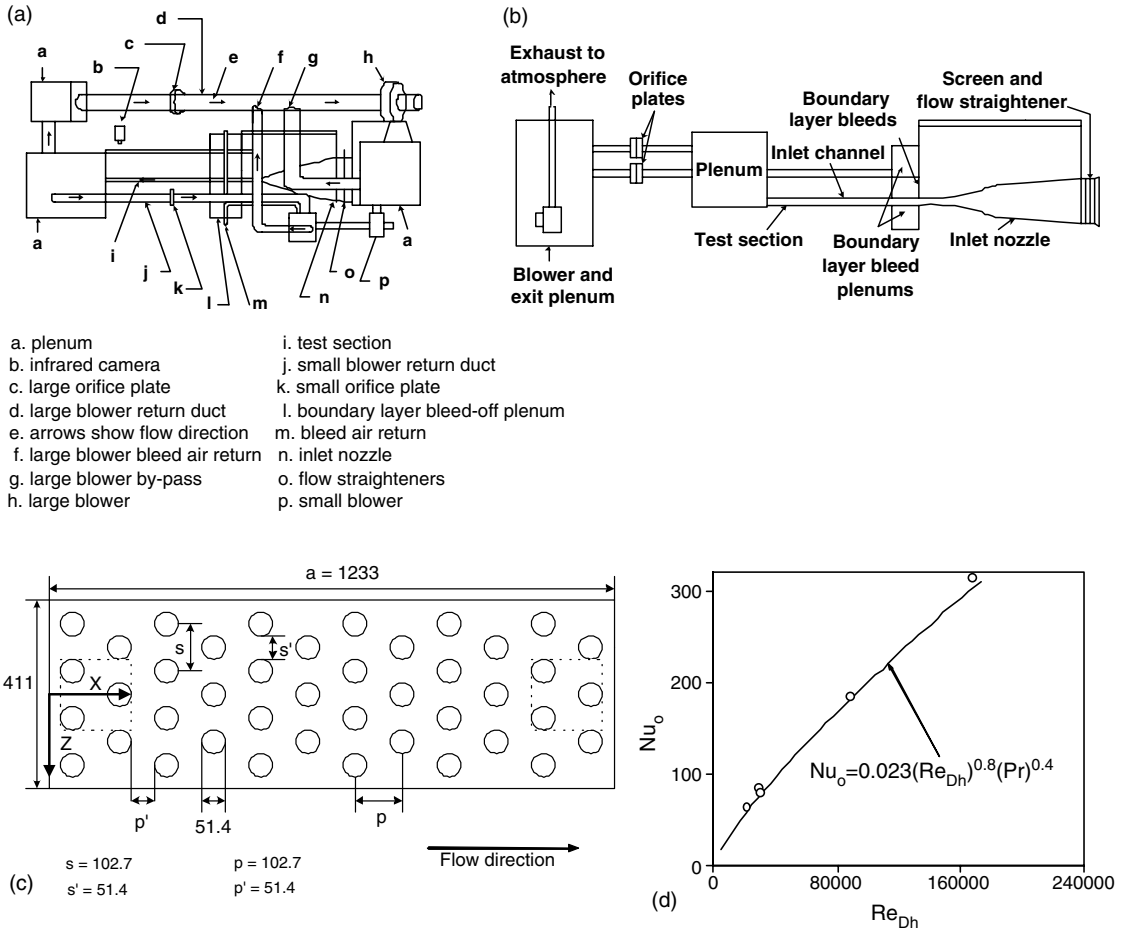

Fig. 1. Schematic diagrams. (a) Facility used for surface heat transfer measurements. (b) Facility used for flow visualization and flow field measurements. (c) The pin fin test section, including coordinate system and dimensions. All dimensions are given in mm. (d) Baseline Nusselt numbers, measured with smooth channel surfaces, no pin fins, and constant heat flux boundary condition, as dependent upon Reynolds number based on hydraulic diameter.

New York Blower Co. 7.5 HP, size 1808 pressure blower. In each case, the air mass flow rate from the test section is measured (upstream of which ever blower is employed) using an ASME standard orifice plate and Validyne M10 digital pressure manometer. The blower then exits into a series of two plenums (0.9 m square and 0.75 m square). A Bonneville cross-flow heat exchanger is located between two of these plenums, and is cooled with liquid nitrogen at flow rate appropriate to give the desired air temperature at the exit of the heat exchanger. As the air exits the heat exchanger, it enters the second plenum, from which the air passes into a rectangular bell mouth inlet, followed by a honeycomb, two screens, and a two-dimensional nozzle with a contraction ratio of 11.2. This nozzles leads to a rectangular cross-section, 411 mm by 50.8 mm inlet duct which is 1219 mm in length. This is equivalent to 13.5 hydraulic diameters (where hydraulic diameter is 90.4 mm). Two trips are employed on the top and bottom surfaces of the inlet duct, just upstream of the test section, which follows with the same cross-section dimensions. It exits to a 0.60 m square plenum, which is followed by two pipes, each containing an orifice plate, mentioned earlier.

Fig. 1c gives the geometric details of the test section, including pin fin geometry. A total of 42 pin fins are used, which extend from the top wall to the bottom wall of the test section. These are placed in a staggered arrangement from one streamwise row to another. The height and diameter d of each pin fin are the same, 51.4 mm. The streamwise and spanwise spacing between pin fin centerlines are each then equal to $2d$. Overall the test section has a height of 51.4 mm (or $1d$), a width of 411.0 mm (or $8d$), and an aspect ratio of 8. The ratio of pin diameter to passage hydraulic diameter is 0.563, and the blockage provided by the first row of pin fins is 50% of the channel cross-sectional area. The top wall of the test section also has two cut-out regions (one at the upstream end and one at the downstream end) where a zinc-selenide window can be installed to allow the infrared camera to view a portion of the test surface on the bottom wall. When this window is not in use, inserts are used in its place. Also identified in Fig. 1c is the test section coordinate system employed for the study. Note that the Y coordinate is directed normal to the bottom wall test surface.

2.2. Local Nusselt number measurement

All exterior surfaces of the facility (between the heat exchanger and test section) are insulated with Styrofoam ($k = 0.024$ W/mK), or 2–3 layers of 2.54 cm thick, Elastomer Products black neoprene foam insulation ($k = 0.038$ W/mK) to minimize heat losses. Calibrated copper-constantan thermocouples are located between the three layers of insulation located beneath the test section to determine conduction losses. Between the first layer and the 3.2 mm thick acrylic test surfaces are custom-made Electrofilm etched-foil heaters (each encapsulated between two thin layers of Kapton) to provide a constant heat flux boundary condition on the test surface. The acrylic surfaces, which are adjacent to the airstream, contain 35 copper-constantan thermocouples, which are placed within the pin fins as well as within the flat portions of the test surface between the pin fins. Each of these thermocouples is located about 0.05 cm just below this surface to provide measurements of local surface temperatures, after correction for thermal contact resistance and temperature drop through the 0.05 cm thickness of acrylic. Acrylic is chosen because of its low thermal conductivity ($k = 0.16$ W/mK at 20 °C) to minimize streamwise and spanwise conduction along the test surface, and thus, minimize "smearing" of spatially varying temperature gradients along the test surface. The power to the foil heater is controlled and regulated using a variac power supply. Energy balances, performed on the heated test surface, then allow determination of local magnitudes of the convective heat flux.

The mixed-mean stagnation temperature of the air entering the test section is measured using five calibrated copper-constantan thermocouples spread across its cross-section. To determine this temperature, thermocouple-measured temperatures are corrected for thermocouple wire conduction losses, channel velocity variations, as well as for the differences between stagnation and recovery temperature. All measurements are obtained when the test facility at steady-state, achieved when each of the temperatures from the thermocouples (on the bottom test surface) vary by less than 0.2 °C over a 10 min period. Thermal conductivity in the Nusselt number is based on the static temperature of the air at the upstream inlet to the test section.

To determine the surface heat flux (used to calculate local heat transfer coefficients and Nusselt numbers), the convective power levels provided by the etched foil heaters are divided by flat test surface areas. Spatially-resolved temperature distributions along the pin fin test surface are determined using infrared imaging in conjunction with thermocouples, energy balances, and in situ calibration procedures. To accomplish this, the infrared radiation emitted by the heated interior surface of the channel is captured using a VideoTherm 340 Infrared Imaging Camera, which operates at infrared wave lengths from 8 to 14 μm. Temperatures, measured using the calibrated, copper-constantan thermocouples distributed along the test surface adjacent to the flow, are used to perform the in situ calibrations simultaneously as the radiation contours from surface temperature variations are recorded.

This is accomplished as the camera views the test surface through a custom-made, zinc-selenide window (which transmits infrared wave lengths between 6 and 17

μm) located on the top wall of the test section. Reflection and radiation from surrounding laboratory sources are minimized using an opaque shield which covers the camera lens and the zinc-selenide window. Frost build-up on the outside of the window is eliminated using a small heated air stream. Eleven to thirteen thermocouple junction locations are usually present in the field viewed by the infrared camera. The exact spatial locations and pixel locations of these thermocouple junctions and the coordinates of a 12.7 cm by 12.7 cm field of view are known from calibration maps obtained prior to measurements. During this procedure, the camera is focused, and rigidly mounted and oriented relative to the test surface in the same way as when radiation contours are recorded.

With these data, gray scale values at pixel locations within video taped images from the infrared imaging camera are readily converted to local surface Nusselt numbers. Because such calibration data depend strongly on camera adjustment, the same brightness, contrast, and aperture camera settings are used to obtain the experimental data. The in situ calibration approach rigorously and accurately accounts for these variations.

Images from the infrared camera are recorded as 8-bit gray scale images on commercial videotape using a Panasonic AG-1960 video recorder. Images are then digitized using NIH Image v1.60 software, operated on a Power Macintosh 7500 PC computer. Subsequent software is used to convert each of 256 possible gray scale values to local Nusselt number values at each pixel location using calibration data. Each individual infrared image covers a 300 pixel by 300 pixel area. Sargent et al. [22] and Mahmood and Ligrani [21] provide additional details of most of the infrared imaging and measurement procedures.

2.3. Time-averaged flow velocity components and pressure

A separate channel facility (but with the same test section), and the same interior geometry identical to that in the heat transfer facility, is employed for flow visualization as well as quantitative surveys of flow structure. This facility is shown schematically in Fig. 1b.

A 1.27 mm diameter miniature five-hole pressure probe, manufactured at the University of Utah especially for these measurements, is used to obtain time-averaged surveys of total pressure, static pressure, and the three mean velocity components. These data are then used to deduce distributions of streamwise vorticity. To obtain the surveys, the probe employed is mounted on an automated two-dimensional traverse, and inserted into the test section from the plenum located just downstream. The output ports of the probe are connected either to Validyne DP103-06 pressure transducers (to measure differential pressures up to 2.5 mm of water), or Celesco LCVR pressure transducers (to measure differential pressures up to 20.0 mm of water). Signals from the transducers are then processed using Celesco CD10D Carrier-Demodulators. Voltages from the Carrier-Demodulators are acquired using a Hewlett–Packard 44422A data acquisition card installed in a Hewlett–Packard 3497A data acquisition control unit. This control unit, the Superior Electric type M092-FD310 Mitas stepping motors on the two-dimensional traverse, a Superior Electric Modulynx Mitas type PMS085-C2AR controller, and a Superior Electric Modulynx Mitas type PMS085-D050 motor drive are controlled by a Hewlett–Packard A4190A Series computer. Contour plots of measured quantities are generated using a polynomial interpolating technique (within DeltaGraph software) between data points. In each survey plane, 1330 data points are spaced 2.54 mm apart. The data at each measurement point is time-averaged over a period of 5 s. Additional details of the five-hole probe measurement procedures, including calibration details, are given by Ligrani et al. [23,24].

2.4. Flow visualization

Flow visualization using smoke is used to identify vortex structures and other secondary flow features. Smoke from four horizontally-oriented smoke wires is employed for this purpose. These are located 12.7, 25.4, and 38.1 mm from the bottom test surface 25–28 mm from the downstream edge of the test section, which is equivalent to $X = 1258$–1261 mm. To accomplish this, each wire is first coated with Barts Pneumatics Corp. super smoke fluid and then powered using a Hewlett–Packard 6433B DC power supply. With this arrangement, the smoke forms into single thin lines parallel to the test surface. As the smoke is advected downstream, the secondary flows which accompany vortex and secondary flow development cause the smoke to be rearranged in patterns which show the locations and distributions of these flow phenomena. Smoke patterns are illuminated in a spanwise-normal light plane located at $X = 1436$ mm using a thin sheet of light provided by a Colotran ellipsoidal No. 550, 1000 W spot light, and a slits machined in two parallel metal plates. Images are recorded using a Panasonic WV-BP330 CCTV video camera, connected to a Panasonic AG-1960 type 4-head, multiplex video cassette recorder. Images recorded on video tape (taken individually or in sequence) are then digitized using a Sony DCR-TRV900 digital video camera recorder. The resulting images are then further processed using a Power Macintosh 7500 PC computer. Additional discussion of many of the procedures used for flow visualization is provided by Ligrani [25].

3. Uncertainty estimates

Uncertainty estimates are based on 95% confidence levels, and determined using procedures described by Kline and McClintock [26] and Moffat [27]. Uncertainty of temperatures measured with thermocouples is 0.15 °C. Spatial and temperature resolutions achieved with the infrared imaging are about 0.52 mm and 0.8 °C, respectively. This magnitude of temperature resolution is due to uncertainty in determining the exact locations of thermocouples with respect to pixel values used for the in situ calibrations. Local Nusselt number ratio uncertainty is then about ±0.13 (for a ratio of 2.00), or about ±6.5%. Reynolds number uncertainty is approximately ±1.8% for Re_H of 13,400. The uncertainties of local total pressure (relative to atmospheric pressure), local static pressure (relative to atmospheric pressure), local streamwise velocity, and local streamwise vorticity are ±4.0%, ±4.0%, ±2.5%, and ±8.0%, respectively.

4. Experimental results and discussion

4.1. Baseline Nusselt numbers

Baseline Nusselt numbers Nu_0, used to normalize the pin fin channel values, are determined from a correlation which matches values measured in a smooth rectangular test section with smooth walls, no pin fins, and an aspect ratio of 4. These measurements are made in the downstream portions of the baseline test section where the channel flow is hydraulically and thermally fully developed. All Nu_0 baseline values are obtained using a T_{oi}/T_w temperature ratio of 0.93–0.95. In addition, baseline measurements are conducted with all four surfaces wrapped with etched foil heaters to provide a heat flux boundary condition around the entire test section. The variation of baseline Nusselt numbers with Reynolds number Re_{Dh} is shown in Fig. 1d. Here, values determined from an average of measurements made on the top and bottom walls, are presented. These values are in agreement with the Dittus-Boelter smooth circular tube correlation [28] for $Re_{Dh} < 180{,}000$.

4.2. Spatially-resolved distributions of local Nusselt numbers

Fig. 2 presents spatially-resolved Nusselt number ratios, measured over about one period of pin fin surface pattern, on the bottom endwall test surface, around and adjacent to the pin fins. The results are given for $Re_H = 50{,}200$ and $T_{oi}/T_w = 0.95$, and are obtained over a measurement area near the upstream portion of the test surface, which extends over X/D_h from 0.3 to 1.6. This is in the vicinity of pins in the first and second rows. In the figure, flow is directed from bottom to top in the increasing X/D_h direction. The data are smoothed slightly, and time-averaged using 25 instantaneous data sets acquired over a period of 25 s.

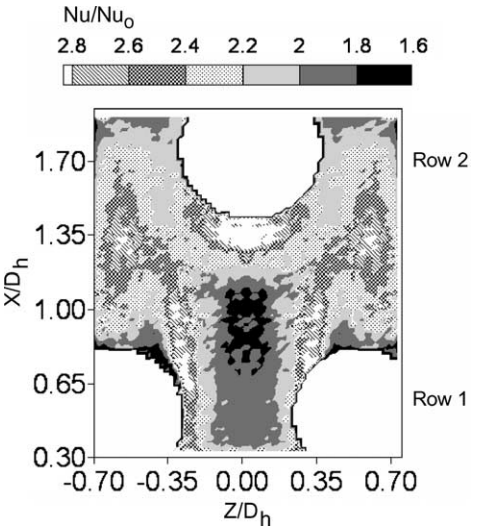

Fig. 2. Spatially-resolved distribution of local Nusselt number ratios Nu/Nu_0 along the endwall test surface, in the upstream portion of the test section, in the vicinity of pin fin rows 1 and 2 for $Re_H = 50{,}200$ and $T_{oi}/T_w = 0.94$.

Nu/Nu_0 variations in Fig. 2 show a number of features which are due to different flow structures which develop because of the presence of the pin fins. One of these is a wake, which forms behind each pin fin. Even though mixing is enhanced, local Nu/Nu_0 are relatively low in the wake region just downstream of the pin fins because of relatively low flow velocities. Farther downstream, local Nu/Nu_0 values increase to become greater than 2.6 as local flow velocities increase, and large-scale unsteadiness forms (with length scales approximately equal to d). These high Nu/Nu_0 regions are evident in Fig. 2 at Z/D_h near −0.5 and +0.5, and for X/D_h from 1.0 to 1.6. At the edges of the wakes, a shear layer is present where the low speed wake flow interfaces with higher speed flow away from the pin fins. Because of the high shear, turbulence production and transport are enhanced, along with local surface Nusselt numbers. The associated augmented Nu/Nu_0 in Fig. 2 are then located along vertical strips over X/D_h from 0.5 to 1.3 which emanate from the spanwise edges of the pins near at Z/D_h of −0.25 and +0.25. A third mechanism for local heat transfer enhancement are the primary and secondary horseshoe vortices which form upstream of each pin fin at the pin-wall junction. The enhancement is a result of the secondary advection provided by this vortex as it advects away from the stagnation line located on the upstream pin fin edge. The secondary advection rearranges cooler fluid, originally located from away from the test surface, so that it is in close proximity with the heated test sur-

face. The resulting Nu/Nu_0 enhancement is evident in Fig. 4 at Z/D_h from −0.3 to +0.3 and at X/D_h from 1.2 to 1.5. Each leg of the primary horseshoe vortex then advects around each side of the adjoining pin fin, and then continues to advect downstream within the shear layers that form near the edges of the pin fin wake.

Because of the streamwise location where the data are obtained in Fig. 2, they are representative of a thermal flow field which is not fully developed. Fig. 3 gives local Nusselt number ratios, also measured for $Re_H = 50{,}200$, at locations further downstream, where X/D_h ranges from 11.7 to 12.9, and the thermal flow field is more fully developed. Here, local Nu/Nu_0 in Fig. 3 are generally lower than values measured in Fig. 2 because of thicker thermal boundary layers. Fig. 3 values also generally have smaller variations at different spatial locations along the test surface. This is because of significant mixing and unsteadiness from the wakes produced by the array of pins located upstream. This mixing and unsteadiness increase progressively as the flow moves downstream through the pin fin array. As a result, three-dimensional advection and turbulent diffusion are enhanced, which causes the vortices to be more diffuse, and shear layers to be less distinct and separate compared to the surrounding flow. Consequently, the local Nu/Nu_0 distribution in Fig. 3 (measured at the downstream portion of the test section) has less distinct and well-defined features compared to the data in Fig. 2 (which is measured at the upstream portion of the test surface). This is especially evident for local Nusselt number variations in Fig. 3 which are beneath the wakes, and beneath the shear layers produced at the edges of these wakes. Also notice that the data in Fig. 2 (for the upstream portion of the test surface) have a larger, more extensive region with relatively lower local Nu/Nu_0 values. Compared to the data in Fig. 3, this region in Fig. 2 is also located farther upstream relative to nearby pin locations.

The effects of Reynolds number on spatially-resolved Nusselt number ratios are apparent if the data in Fig. 4 for $Re_H = 13{,}400$ are compared to the data in Fig. 3 for $Re_H = 50{,}200$. The data presented in both figures are measured on the same downstream part of the test surface (where the thermal flow field is fully developed) for T_{oi}/T_w of 0.94–0.95. The results shown in Figs. 3 and 4 are also time-averaged using 25 instantaneous data sets. Comparison shows that local Nu/Nu_0 data on the bottom wall of the test surface (around and away from the pin fins) are generally lower at a given location as Re_H increases, a conclusion also supported by measurements made at Re_H of 18,700, 81,900, and 110,900. However, regardless of the Reynolds number, Nusselt number ratios are locally augmented beneath the horseshoe vortices, and beneath the shear layers at the edges of the wakes. Local Nu/Nu_0 augmentations are less apparent beneath the central parts of pin fin wakes, especially as Re_H increases, because of increased mixing, advection, and diffusion caused by the wakes from upstream pin fins.

4.3. Local instantaneous and time-averaged flow structure

An instantaneous flow visualization image is presented in Fig. 5 for $Re_H = 430$, which is illuminated downstream of the pin fin test section at $X = 1436$ mm. The wires used to produce the smoke are located at $X = 1258$–1261 mm. These locations are about 25.1 and 203.1 mm downstream of the pin fin test section, respectively. The data in Fig. 5 are obtained at this low

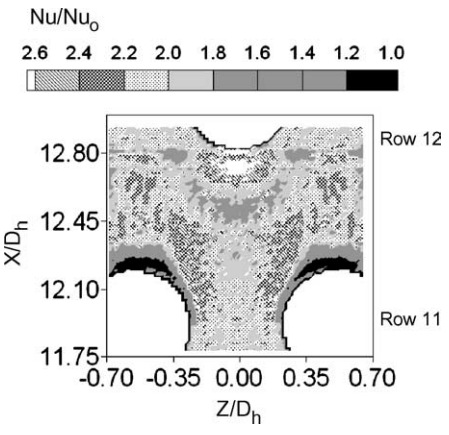

Fig. 3. Spatially-resolved distribution of local Nusselt number ratios Nu/Nu_0 along the endwall test surface, in the downstream portion of the test section, in the vicinity of pin fin rows 11 and 12 for $Re_H = 50{,}200$ and $T_{oi}/T_w = 0.94$.

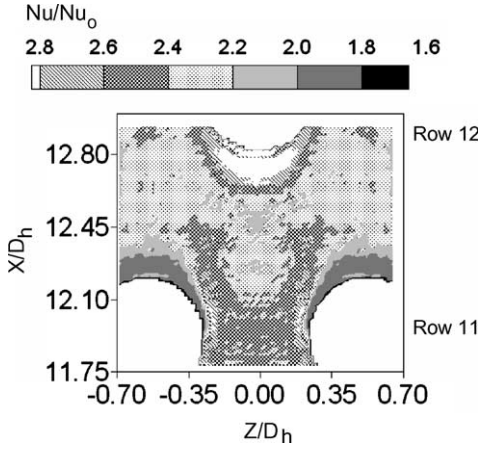

Fig. 4. Spatially-resolved distribution of local Nusselt number ratios Nu/Nu_0 along the endwall test surface, in the downstream portion of the test section, in the vicinity of pin fin rows 11 and 12 for $Re_H = 13{,}400$ and $T_{oi}/T_w = 0.92$.

Reynolds number because diffusion and increased unsteadiness at higher Reynolds numbers result in smeared and unrecognizable flow patterns. The image extends in the vertical direction from the bottom to the top of the channel, and in the horizontal direction over a distance of about 2.5 channel heights. The spanwise center of each image is then located at the spanwise center of the test section at $Z/D_h = 0$. The most important features in each image are two large, primary vortex pairs (indicated by mushroom-shaped smoke patterns). One of these is on the right-side of the image, and one is on the left side of the image in Fig. 5. The one on the right has an upwash region directed downwards from the top wall, and the one on the left has an upwash region directed upwards with respect to the bottom wall. The two primary vortex pairs are formed by the blockage and streamline displacement effects of the pin fins, and are the remnants (or downstream manifestations) of the two legs of the horseshoe vortices which initially form just upstream of individual pins. Fig. 5 provides evidence that the secondary flows within and around these vortices are especially intense, as indicated by different convolutions and distortions of smoke patterns.

These same two dominant vortex pairs are believed to be present at approximately the same channel locations over a range of Reynolds numbers Re_H, including ones corresponding to fully turbulent flow. This is because the same mechanisms which initially produce the vortex pairs (i.e. local pressure gradients just upstream of individual pins) are present over a wide range of Reynolds numbers. Note that the orientations of the primary vortex pairs sometimes change substantially as time proceeds. This is because each vortex signature is surrounded by complex, unsteady secondary flows, which also rearrange distributions of streamwise velocity. As a result, shear gradients and mixing are spread over the entire channel cross-section. Such behavior aids convective processes for heat transfer augmentation by: (i) increasing secondary advection of fluid between the central parts of the channel and regions near the wall, and (ii) producing regions with high, three-dimensional shear and high magnitudes of turbulence production over much of the channel cross-section, thereby substantially increasing turbulence transport levels in all three coordinate directions.

Time-averaged data also provide evidence of significant mixing and pairs of counter-rotating vortices in the pin fin channel. These data are presented in Figs. 6–8, and are measured at Re_H of 6000, 8000, and 10,000 and $X = 1235$ mm, which is located 2.1 mm immediately downstream of the last row of pins in the test section. The surveys, presented in Fig. 6, are made over a spanwise-normal plane, which extends about one channel height in the vertical direction, and about 3.5 channel heights in the horizontal direction.

Evidence of vortex pairs produced by the pin fins is provided by regions of positive and negative streamwise vorticity, which are adjacent to each other, in the time-averaged streamwise vorticity survey shown in Fig. 6e. In this figure, the strongest of these vortex signatures are positioned just downstream of the central pin at $Z/H = -0.5$ to $+0.5$. These regions of augmented vorticity are located near the edges of the shear layer, evident in the surveys of local streamwise velocity and local total pressure in Fig. 6a and b, respectively. Such shear layers form at the edges of the wakes which develop behind individual pin fins. In this case, they are present downstream of the farthest downstream row of pin fins. The static pressure survey in Fig. 6c shows different variations which are mostly a result of the curvature of the streamlines which develop downstream of the pin fin array. The survey of time-averaged spanwise velocity component in Fig. 6d also shows large variations in the shear layers produced at the edges of the wake from the central pin fin. This figure shows spanwise velocity components moving in the $-Z$ direction in the right shear layer behind the central pin fin (at Z/H from 0 to $+1.0$), and in the $+Z$ direction in the left shear layer behind the central pin fin (at Z/H from 0 to -1.0).

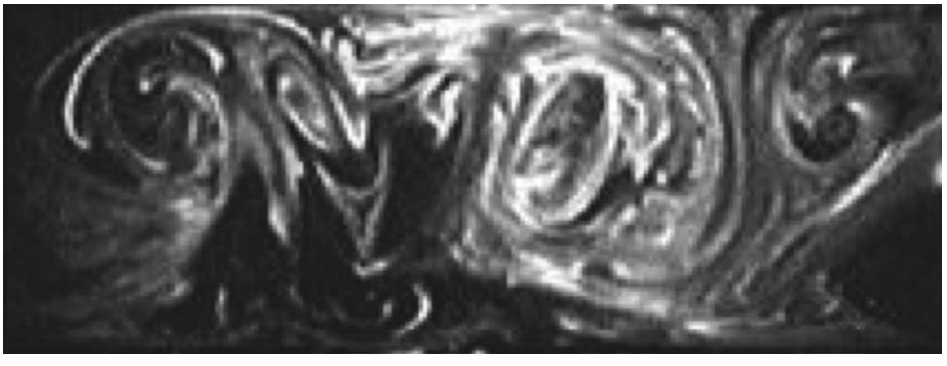

Fig. 5. Instantaneous flow visualization image illuminated on a spanwise-normal light plane located at $X = 1436$ mm for $Re_H = 430$.

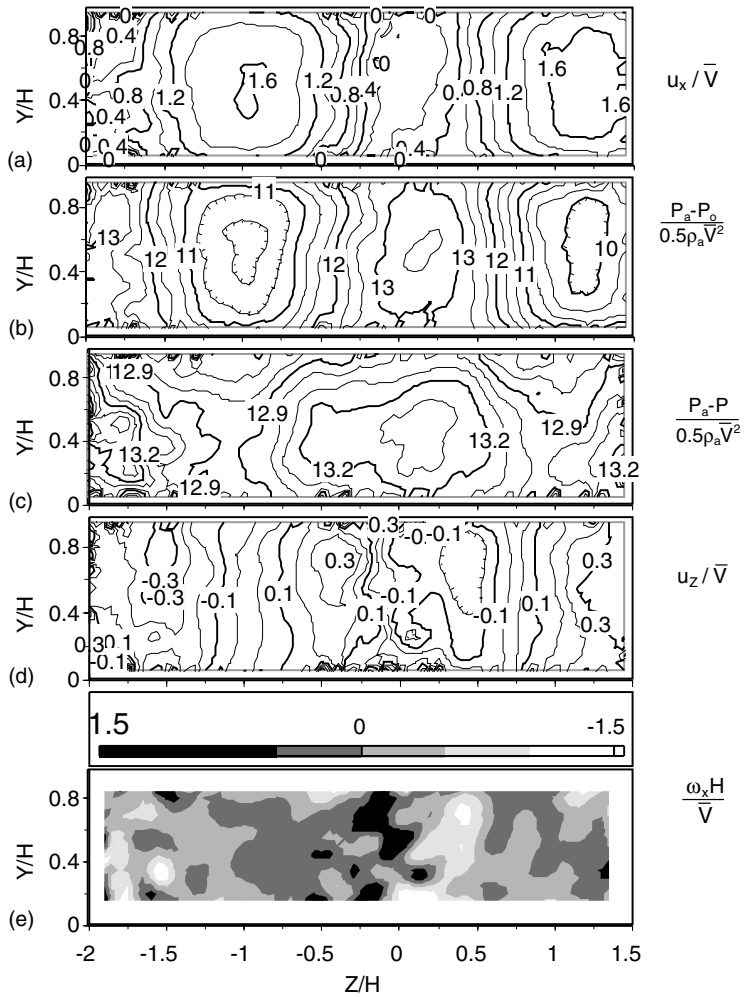

Fig. 6. Time-averaged surveys of flow field properties measured in a spanwise-normal plane located at $X = 1235$ mm for $Re_H = 8000$.

Fig. 7 presents profiles of spanwise-averaged magnitudes of streamwise velocity, total pressure deficits, and static pressure deficits, as dependent upon Y/H, which are deduced from survey results like the ones presented in Fig. 6. Dimensional magnitudes are given in Fig. 7a–c, and normalized values are given in Fig. 7d–f for different Reynolds numbers. In these figures, total and static pressure deficits are reasonably uniform across the height of the channel, whereas the streamwise velocity shows important deficits near the top and bottom walls. Note that the $\overline{U}$ values used to normalize the data in Figs. 7d–f and 8f–j is based on the average mass flow rate in the channel.

Fig. 8 gives profiles of magnitudes of the same quantities which are presented in Fig. 6. These data are averaged in the normal direction and shown as they vary with Z/H. Dimensional magnitudes are presented in Fig. 8a–e, and normalized magnitudes are given in Fig. 8f–j for different Reynolds numbers. Measurements show that the variations shown in these figures repeat themselves across the span of the channel as the wakes from additional pin fins are encountered. Substantial deficits of streamwise velocity and total pressure are evident immediately downstream of the central pin in the farthest downstream row of pins. Deficits of static pressure are also present at the same location, but are less substantial on a percentage basis. Note that the spanwise velocity component u_z is negative in the right shear layer behind the central pin fin (at Z/H from 0 to +1.2), and positive in the left shear layer behind the central pin fin (at Z/H from 0 to −1.2). Streamwise vorticity variations in Fig. 8e and j also shows interesting variations over the same range of locations, with positive values and then negative values, as Z/H increases and the wake is traversed.

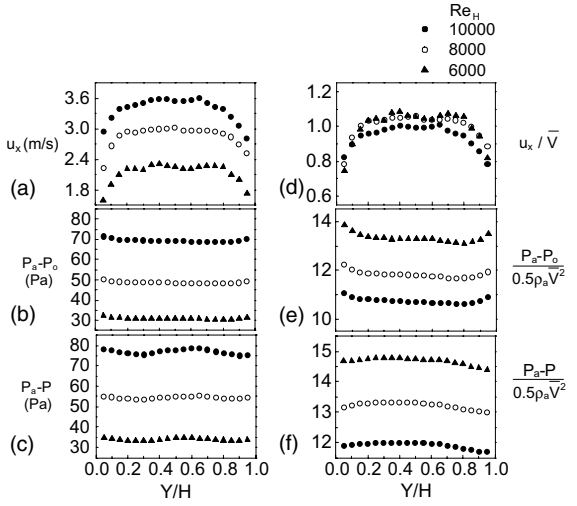

Fig. 7. Normalized and dimensional profiles of flow field properties measured in a spanwise-normal plane located at $X = 1235$ mm, and averaged in the spanwise direction, for different Re_H.

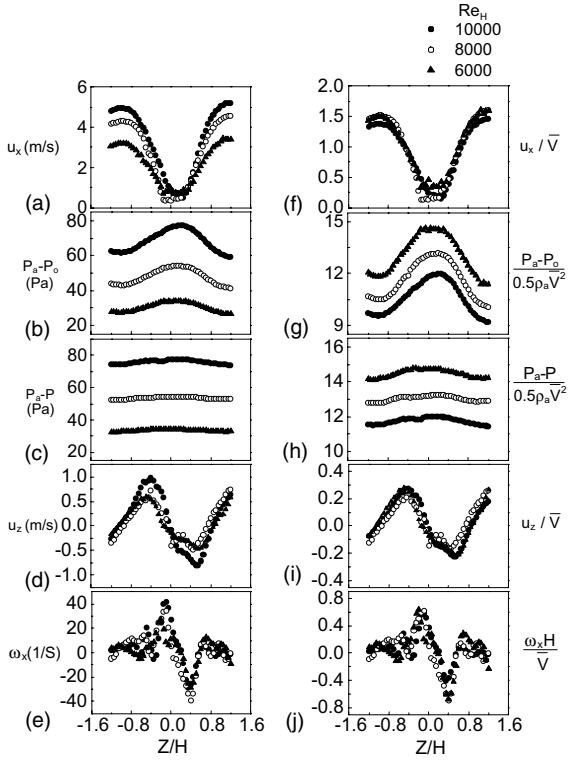

Fig. 8. Normalized and dimensional profiles of flow field properties measured in a spanwise-normal plane located at $X = 1235$ mm, and averaged in the normal direction, for different Re_H.

4.4. Effects of Reynolds number and streamwise development on local Nusselt number ratio variations

The results presented in Figs. 9a, b and 10a, b provide additional information on the effects of Reynolds number and streamwise development on local Nu/Nu_0 distributions. The local Nusselt number ratios presented in the last three of these figures are obtained either along a line of constant X/D_h, or along a line of constant Z/D_h. The locations of these lines are shown in Fig. 9a. All of these data are obtained from survey results (such as the ones shown in Figs. 2–4) at Re_H ranging from 13,400 to 110,900, at about constant temperature ratio T_{oi}/T_w of 0.92–0.96.

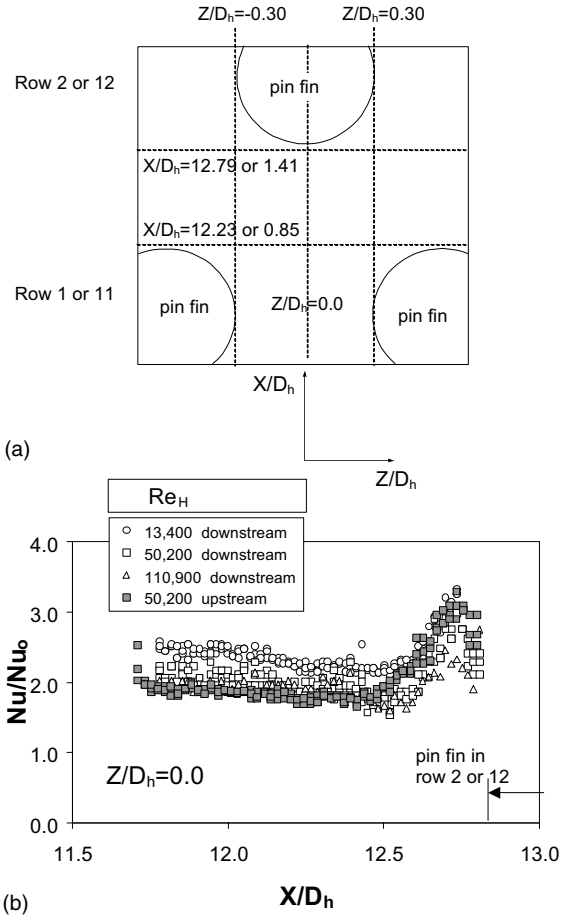

Fig. 9. (a) Non-dimensional spatial locations relative to pin fin locations for the upstream and downstream measurement regions. Also shown are locations where the data in (b), Fig. 10a, b are presented. (b) Local Nusselt number ratios Nu/Nu_0 along the bottom endwall test surface at $Z/D_h = 0.00$ for different Reynolds numbers Re_H and for a temperature ratio T_{oi}/T_w of 0.92–0.96.

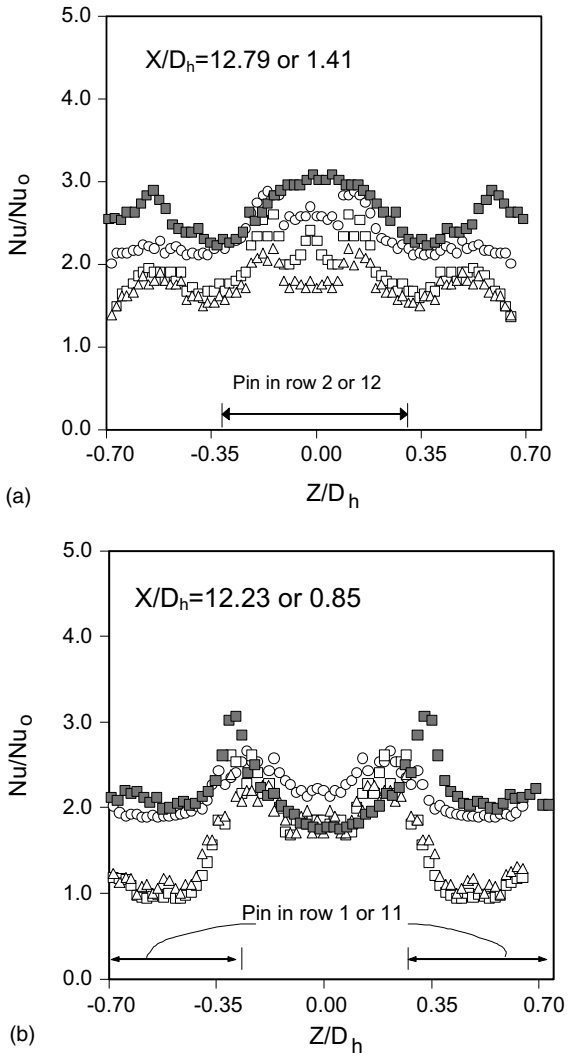

Fig. 10. Local Nusselt number ratios Nu/Nu_0 along the bottom endwall test surface for different Reynolds numbers Re_H and for a temperature ratio T_{oi}/T_w of 0.92–0.96. Symbols are defined in Fig. 9b. (a) Data given at $X/D_h = 12.79$ for the downstream measurement area, and at $X/D_h = 1.41$ for the upstream measurement area. (b) Data given at $X/D_h = 12.23$ for the downstream measurement area, and at $X/D_h = 0.85$ for the upstream measurement area.

In Fig. 9b, local Nu/Nu_0 data are given as they vary with X/D_h for constant $Z/D_h = 0.0$ to illustrate endwall surface behavior beneath the horseshoe vortices. Here, local Nu/Nu_0 values at X/D_h from 11.70 to 12.85 correspond to locations *upstream* of the central pin fin in the 12th row. If the first three data sets, measured at downstream locations, are considered, local Nusselt number ratios generally decrease at most all streamwise locations as the Reynolds number increases. The effects of the horseshoe vortex on local Nusselt number ratios are apparent at X/D_h from 12.60 to 12.85, where local Nu/Nu_0 are augmented considerably compared to upstream locations. The effects of streamwise development are apparent if the two data sets measured at upstream and downstream locations at $Re_H = 50{,}200$ are considered. Note that the upstream data are displaced an X/D_h distance of 11.38 on this plot. Comparison of these two data sets shows higher values for the upstream measurements in the regions where the horseshoe vortices are most influential. The is partially due to greater levels of vorticity diffusion and mixing at the downstream location, which seems to cause the horseshoe vortices to be more diffuse and less energetic in augmenting thermal transport.

Similar variations due to the horseshoe vortex, located just in front of a pin fin positioned in the 12th row, are also apparent at Z/D_h from −0.3 to +0.3 in Fig. 10a. Here, local Nu/Nu_0 data are given as they vary with Z/D_h for constant $X/D_h = 12.79$ for the downstream data set, and for constant $X/D_h = 1.41$ for the upstream data set. Referring to the data measured at downstream locations for Re_H of 13400, 50200, and 110,900, the effects of the primary and secondary horseshoe vortices are complex, as indicated by locally higher Nu/Nu_0 values at $Z/D_h = +0.15$ to +0.20, and at $Z/D_h = -0.15$ to −0.20. Values are then locally lower between these two regions at each Reynolds number. The results in Fig. 10a also illustrate surface behavior beneath the downstream parts of the wakes and shear layers produced by pin fins in the eleventh row. Similar variations due these phenomena are evident on both sides of Fig. 10a at Z/D_h in the vicinity of +0.50 and −0.50.

As for the results in the previous figure, the effects of streamwise development are apparent in Fig. 10a if the two data sets measured at upstream and downstream locations at $Re_H = 50{,}200$ are considered. Comparison of these two data sets again shows that upstream measurement area values are generally higher than the values measured over the downstream measurement area. The horseshoe vortex also appears to produce different local behavior for these two regions. In particular, a broad local Nu/Nu_0 augmented region is present for the upstream location, whereas a more complicated series of local maximum and local minimum Nu/Nu_0 values are present for the downstream measurement location.

The Nu/Nu_0 data in Fig. 10b are given as they vary with Z/D_h for constant X/D_h of 12.23 and 0.85 to illustrate surface behavior beneath the wakes produced by the pin fins located in the 11th row, and shear layers which form near the edges of these wakes. In Fig. 10b, the pin fins in the 11th row are located at $Z/D_h < -0.30$, and $Z/D_h > 0.30$. The results in this figure again generally indicate that local Nusselt number ratios decrease as the Reynolds number increases at most Z/D_h locations. The effects of the shear layers are most evident at $Z/D_h = -0.15$ to −0.35 and $Z/D_h = +0.15$ to +0.35 for

downstream measurement locations, and at $Z/D_h = -0.25$ to -0.45 and $Z/D_h = +0.25$ to $+0.45$ for upstream measurement locations. Local Nusselt number ratios are locally augmented at these positions compared to other Z/D_h positions as a result of the increased shear and turbulence transport levels. Fig. 10b also shows that the effects of streamwise development for $Re_H = 50, 200$ are most apparent within the shear layers and on the parts of the test surface away from and outside of the pin fin wakes. This is because values measured over upstream and downstream regions at this Reynolds number are about the same within the wake at Z/D_h from -0.25 to $+0.25$.

Overall, the results in Figs. 9 and 10 show that local Nusselt number ratios generally decrease somewhat on the flat regions away from the pin fins as Re_H increases. Because of the normalization employed, this means that the observed Nusselt number Nu increases with Reynolds number are at a lower rate than baseline Nu_0 increases with Re_{Dh}. In all cases, Nu/Nu_0 values in Figs. 9 and 10 are generally much higher than 1.0 on most of the test surface, including the flat regions between the pin fins, irrespective of the value of Reynolds number employed.

5. Summary and conclusions

Spatially-resolved local Nusselt numbers are highest beneath primary and secondary horseshoe vortices located just upstream of individual pins, beneath pin wakes, and on just downstream of the pins, in regions where shear layers are positioned between the wakes behind the pins and the higher speed flow away from an individual pin. Also important are intense, highly unsteady secondary flows and vortex pairs (evident in flow visualizations and time-averaged surveys of streamwise vorticity), which increase secondary advection and turbulent transport over the entire channel cross-section. The resulting local Nusselt number ratios (pin fin Nusselt numbers normalized by values measured in a smooth channel) are augmented compared to channels with no pin fins and smooth walls, and vary significantly with Reynolds number.

Acknowledgements

The work presented in this paper was sponsored by a AGTSR Advanced Gas Turbine Research Program research subcontract sponsored by the US Department of Energy—National Energy Technology Laboratory through a cooperative agreement with the South Carolina Institute for Energy Studies at Clemson University. Mr. Jeff Harrison and Mr. Eli Comeau helped in processing some of the data, and in setting up the experimental apparatus employed in the investigation.

References

[1] A. Zukauskas, Heat transfer from tubes in cross flow, Adv. Heat Transfer 8 (1972) 96–160.
[2] E.M. Sparrow, J.W. Ramsey, C.A.C. Altemani, Experiments on in-line pin fin arrays and performance comparisons with staggered array, ASME Trans.—J. Heat Transfer 102 (1) (1980) 44–50.
[3] D.E. Metzger, S.W. Haley, Heat transfer experiments and flow visualization for arrays of short pin-fins, ASME Paper No. 82-GT-138, 1982.
[4] D.E. Metzger, R.A. Barry, J.P. Bronson, Developing heat transfer in rectangular ducts with staggered arrays of short pin-fins, ASME Trans.—J. Heat Transfer 104 (4) (1982) 700–706.
[5] G.J. Van Fossen, Heat-transfer coefficients for staggered arrays of short pin-fins, ASME Trans.—J. Eng. Power 104 (2) (1982) 268–274.
[6] A.W. Brigham, G.J. Van Fossen, Length to diameter ratio and row number effects in short pin fin heat transfer, ASME Trans.—J. Eng. Gas Turbines Power 106 (1) (1984) 241–245.
[7] R.J. Simoneau, G.J. Van Fossen, Effects of location in an array on heat transfer to a short cylinder in cross flow, ASME Trans.—J. Heat Transfer 106 (1) (1984) 42–48.
[8] S.C. Lau, J.C. Han, Y.S. Kim, Turbulent heat transfer and friction in pin fin channels with lateral flow ejection, ASME Trans.—J. Heat Transfer 111 (1) (1989) 51–58.
[9] R.D. McMillin, S.C. Lau, Effects of trailing-edge ejection on local heat (mass) transfer in pin fin cooling channels in turbine blades, ASME Trans.—J. Turbomachinery 116 (1) (1994) 159–168.
[10] M.K. Chyu, Heat transfer and pressure drop for short pin-fin arrays with pin-endwall fillet, ASME Trans.—J. Heat Transfer 112 (4) (1990) 926–932.
[11] M.K. Chyu, R.J. Goldstein, Influence of an array of wall-mounted cylinders on the mass transfer from a flat surface, Int. J. Heat Mass Transfer 34 (9) (1991) 2175–2186.
[12] M.K. Chyu, Y.C. Hsing, T.I.-P. Shih, V. Natarajan, Heat transfer contributions of pins and endwall in pin-fin arrays: effects of thermal boundary condition modeling, ASME Trans.—J. Turbomachinery 121 (2) (1999) 257–263.
[13] V.B. Grannis, E.M. Sparrow, Numerical simulation of fluid flow through an array of diamond shaped pin fins, Numer. Heat Transfer, Part A 19 (1991) 381–403.
[14] D.A. Olson, Heat transfer in thin, compact heat exchangers with circular, rectangular, or pin-fin flow passages, ASME Trans.—J. Heat Transfer 114 (2) (1992) 373–382.
[15] M.K. Chyu, V. Natarajan, Heat transfer on the base surface of three-dimensional protruding elements, Int. J. Heat Mass Transfer 39 (14) (1996) 2925–2935.
[16] M.K. Chyu, Y.C. Hsing, V. Natarajan, Convective heat transfer of cubic fin arrays in a narrow channel, ASME Trans.—J. Turbomachinery 120 (2) (1998) 362–367.
[17] J.J. Hwang, C.C. Lu, Lateral-flow effect on endwall heat transfer and pressure drop in a pin-fin trapezoidal duct of various pin shapes, ASME Paper No. 2000-GT-232, 2000.

[18] O. Uzol, C. Camci, Elliptical pin fins as an alternative to circular pin fins for gas turbine blade cooling applications. Part 1: endwall heat transfer and total pressure loss characteristics, ASME Paper No. 2001-GT-180, 2001.

[19] O. Uzol, C. Camci, Elliptical pin fins as an alternative to circular pin fins for gas turbine blade cooling applications. Part 2: wake flow field measurements and visualization using particle image velocimetry, ASME Paper No. 2001-GT-181, 2001.

[20] A.M. Al Dabagh, G.E. Andrews, Pin-fin heat transfer: contribution of the wall and the pin to the overall heat transfer, ASME Paper No. 92-GT-242, 1992.

[21] G.I. Mahmood, P.M. Ligrani, Heat transfer in a dimpled channel: combined influences of aspect ratio, temperature ratio, Reynolds number, and flow structure, Int. J. Heat Mass Transfer 45 (10) (2002) 2011–2020.

[22] S.R. Sargent, C.R. Hedlund, P.M. Ligrani, An infrared thermography imaging system for convective heat transfer measurements in complex flows, Measure. Sci. Technol. 9 (12) (1998) 1974–1981.

[23] P.M. Ligrani, B.A. Singer, L.R. Baun, Miniature five-hole pressure probe for measurement of three mean velocity components in low speed flow, J. Phys. E—Sci. Instrum. 22 (10) (1989) 868–876.

[24] P.M. Ligrani, B.A. Singer, L.R. Baun, Spatial resolution and downwash velocity corrections for multiple-hole pressure probes in complex flows, Exp. Fluids 7 (6) (1989) 424–426.

[25] P.M. Ligrani, Flow visualization and flow tracking as applied to turbine components in gas turbine engines, Measure. Sci. Technol. 11 (7) (2000) 992–1006.

[26] S.J. Kline, F.A. McClintock, Describing uncertainties in single sample experiments, Mech. Eng. 75 (1953) 3–8.

[27] R.J. Moffat, Describing the uncertainties in experimental results, Exp. Thermal Fluid Sci. 1 (1) (1988) 3–17.

[28] J.H. Lienhard, A Heat Transfer Textbook, second ed., Prentice-Hall, Englewood Cliffs, NJ, 1987.